New Insights into Interfacial Passivation on 3D Graphene–$CuInS_2$ Composites-Based Perovskite Solar Cells

Gao, Feng; Hong, Weihua; Zhao, Ziying; Zhang, Chao; Deng, Xiaoting; Cao, Jiamin; Yu, Donghong

Published in:
Solar RRL

DOI (link to publication from Publisher):
10.1002/solr.202300166

Publication date:
2023

Document Version
Publisher's PDF, also known as Version of record

Solar RRL
www.solar-rrl.com

New Insights into Interfacial Passivation on 3D Graphene–$CuInS_2$ Composites-Based Perovskite Solar Cells

Feng Gao, Weihua Hong, Ziying Zhao, Chao Zhang, Xiaoting Deng, Jiamin Cao,* and Donghong Yu**

Although it is generally accepted by the perovskite solar cells community that their interface behaviors have a profound impact on their power conversion efficiency (PCE) and stability, such interfacial engineering on the bottom interface between electron transport layer (ETL) and perovskite film is still lagging. Herein, a 3D graphene (G)–$CuInS_2$ composite is designed as an efficient ETL to improve both the interfacial contact and passivate defects at the G–$CuInS_2$/perovskite interface. The lattice matching of graphene and methylammonium lead iodide $CH_3NH_3PbI_3$ inhibits the concentrated stress generated during the growth of perovskite, resulting in crystal films with large grain boundaries. The low-electron defect density in 3D G–$CuInS_2$ composite facilitates the electron transport from perovskite film to $CuInS_2$ quantum dots. In addition, 3D G–$CuInS_2$ shows excellent carrier extraction capability of reducing carrier extraction time by 1.47 times than that of the counterpart. Correspondingly, a highly improved PCE of 22.4% is obtained, which increases by 15% of the counterpart. Furthermore, the unencapsulated device based on 3D G–$CuInS_2$ shows long-term stability, maintaining 85% of its original efficiency in air for 30 days. This strategy provides a new route to interfacial passivation engineering for preparation of high-performance perovskite solar cells.

1. Introduction

Recently, perovskite solar cells (PSCs) have achieved important progress in performance with power conversion efficiency (PCE) up to 25%,[1–3] which are considered to be one of the most promising large-scale photovoltaic devices for future energy supplies. Their high efficiency benefits from effective charge extraction through nonradiative recombination during the charge transport at the perovskite interfaces,[2,4,5] between hole transport layer and perovskite, which can be significantly reduced by passivating the top contact surface with the use of organic halide salts.[6] However, few reports on perovskite bottom interface passivation have been explored due to solvent incompatibility and demands of high-temperature treatment. Being one of the crucial charge transport layers for perovskite devices, an electron transport layer (ETL) plays a key role in extracting and transporting those photogenerated electrons.[7–9] Therefore, developing new types of ETLs that can passivate the bottom of the perovskite layer has become an imminent scientific challenge. At present, the commonly used ETL materials such as TiO_2,[10–13] SnO_2,[14–16] and some C_{60} derivatives[17] have not acquired satisfactory passivation effects yet in PSCs community.

$CuInS_2$ quantum dots (QDs) has been considered as an outstanding light-harvesting material for PSCs due to their unique properties, such as low direct bandgap, high absorption coeffcient ($\alpha = 5 \times 105\ cm^{-1}$), low toxicity, and so on,[18,19] which are usually in forms of colloidal particles. Due to van der Waals

F. Gao, W. Hong, Z. Zhao, C. Zhang, X. Deng
School of Food and Chemical Engineering
Shaoyang University
Shaoyang 422000, P. R. China
E-mail: gaofeng137@tju.edu.cn

J. Cao
Key Laboratory of Theoretical Organic Chemistry and Functional Molecule of Ministry of Education
Hunan Provincial Key Laboratory of Controllable Preparation and Functional Application of Fine Polymers
School of Chemistry and Chemical Engineering
Hunan University of Science and Technology
Xiangtan 411201, P. R. China
E-mail: jiamincao@hnust.edu.cn

D. Yu
Department of Chemistry and Bioscience
Aalborg University
DK-9220 Aalborg East, Denmark
E-mail: yu@bio.aau.dk

D. Yu
Sino-Danish Center for Education and Research
DK-8000 Aarhus, Denmark

The ORCID identification number(s) for the author(s) of this article can be found under https://doi.org/10.1002/solr.202300166.

DOI: 10.1002/solr.202300166

interaction among them, those nanoparticles are unstable, tending to form large agglomerates and thus reducing the quality of film formation.[20] To overcome that, in our previous work, $CuInS_2$ QDs were once modified with graphene sheet to form 2D composites, which successfully provided a charge transfer tunnel for photogenerated carriers.[9] However it should be noted that, during the preparation of the PSCs, such graphene-modified $CuInS_2$ was applied by blending them with the perovskite precursor, resulting in unsatisfactory formation of individual thin films of $CuInS_2$ QDs. As a result, the mechanism of interface passivation between perovskite, $CuInS_2$, and graphene was not completely studied.

Herein, we adopted inorganic ammonium salt to ameliorate the formation of 3D graphene–$CuInS_2$ composite (3D G–$CuInS_2$) by generating gaseous ammonia during the reduction of graphene oxide (GO). Different from our previous work, the as-synthesized 3D G–$CuInS_2$ this time was directly applied as an ETL as a new device structure so as to study the interface passivation between perovskite crystal and 3D G–$CuInS_2$. In such 3D G–$CuInS_2$ composites, the strong interaction between curved graphene and $CuInS_2$ QDs improved the dispersion of particles within the composite and reduced the influence of their aggregation on the film formation. Besides, the well-matched graphene and perovskite lattice would suppress stress concentration during crystal growth, while the functional groups in G–$CuInS_2$ composites passivated the excess Pb in methylammonium lead iodide ($MAPbI_3$), decreasing the carrier recombination at the interface between the $CuInS_2$ and $MAPbI_3$. Based on various favorable factors, we obtained a $MAPbI_3$ solar cell with an outstanding PCE of 22.4% with an increase of 15% of that of the pristine $CuInS_2$ counterpart.

2. Results and Discussion

Graphene oxide used in our work was a transparent, flexible, and flake-like material (as shown in Figure S1, Supporting Information). As shown in transmission electron microscopy (TEM)/high resolution transmission electron microscopy

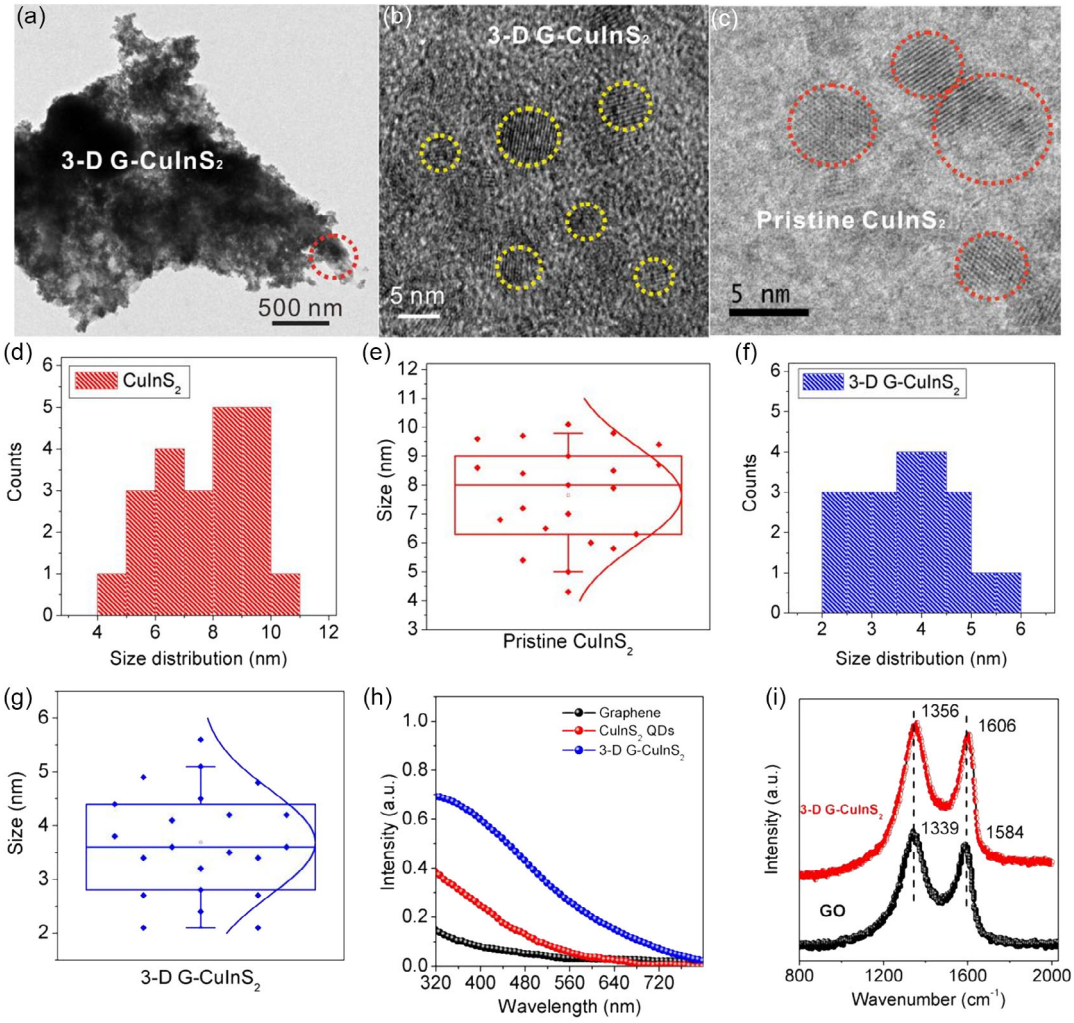

Figure 1. a) TEM image of 3D G–$CuInS_2$. b) Zoomed-in HRTEM image of selected area (red circled) in (a). c) HRTEM of pristine $CuInS_2$. d–e) The size distribution of pristine $CuInS_2$. f–g) The size distribution of $CuInS_2$ in 3D G–$CuInS_2$ composite. h) UV–vis absorption spectra of the samples. i) The Raman spectra of graphene oxide and 3D G–$CuInS_2$.

(HRTEM) images (**Figure 1**a, S2b, Supporting Information and Figure 1b), the obtained 3D G–$CuInS_2$ QDs are firmly bound at the graphene surface to form a stable composite without any other substance in the blank region outside the composite, indicating their strong interactions in the reaction process. This was in fact furthermore proved by our Raman studies, as presented in Figure 1h, whereas graphene oxide exhibits its typical G band with the Raman shift at 1584 cm^{-1} (associated with the vibration of sp^2-bonded carbon atoms) and D band at 1339 cm^{-1} (correlated to vibrations of carbon atoms with dangling bonds). The D band and G band are redshifted to 1356 and 1606 cm^{-1} in 3D G–$CuInS_2$ respectively, suggesting that the graphene sheets are very likely single layered. Furthermore, the intensity ratio of I_D/I_G for 3D G–$CuInS_2$ composite decreased, inferring a well-recovered defect in graphene sheets during the reaction process.[21] Meanwhile, the absorption spectra of 3D G–$CuInS_2$ composite exhibited in Figure 1h pronounces a much higher absorption than the pristine $CuInS_2$ and graphene at the region of 300–800 nm. Figure 1c and S2a, Supporting Information shows the HRTEM images of pristine $CuInS_2$ QDs, with a size distribution of 4–10 nm (Figure 1d,e), larger than those of 3D G–$CuInS_2$ composites in 2–6 nm (Figure 1f,g and **2**c). The crystallite size of $CuInS_2$ particles in the 3D G–$CuInS_2$ is calculated to be 2–5 nm using the Scherrer formula (corresponding XRD patterns shown in Figure S3, Supporting Information),[10] which is consistent with the TEM result. As literature reported, the oxygen-containing functional groups on the surface of graphene have strong effects on crystal growth, leading to the fact that the nanoparticles decorated on graphene become smaller with more narrow distribution.[9,22,23] All these reveal that graphene can retard the growth of both crystals and QDs.

To investigate the entire synthesis process of 3D G–$CuInS_2$, a TEM study on morphological changes of the composites at different reaction times of 1, 3, and 6 h is captured, respectively (Figure 2a–c). At the first stage of the reaction within 1 h, $CuInS_2$ QDs were well dispersed on the graphene sheet surface. In this period, ions are trapped from solution by graphene surface defects, leading to the preliminarily formation of $CuInS_2$ QDs.[9] When reaching 3 h of this reaction, the graphene sheet became fully covered by those QDs. During this period, ammonium ions release gaseous ammonia at high temperature, resulting in curling of the parts of graphene sheets and self-encapsulation which must be thermodynamically driven. When the reaction time reached 6 h, certain graphene sheets completely curled into a 3D composite structure (**Figure 3**c) with $CuInS_2$ QDs densely stacked on them. The growth diagram of the 3D G–$CuInS_2$ is found in Figure 1d.

The SEM images of $MAPbI_3$ on different substrates are characterized to further study the crystal morphology. The $MAPbI_3$ crystallites on pristine $CuInS_2$ substrate were concluded to be

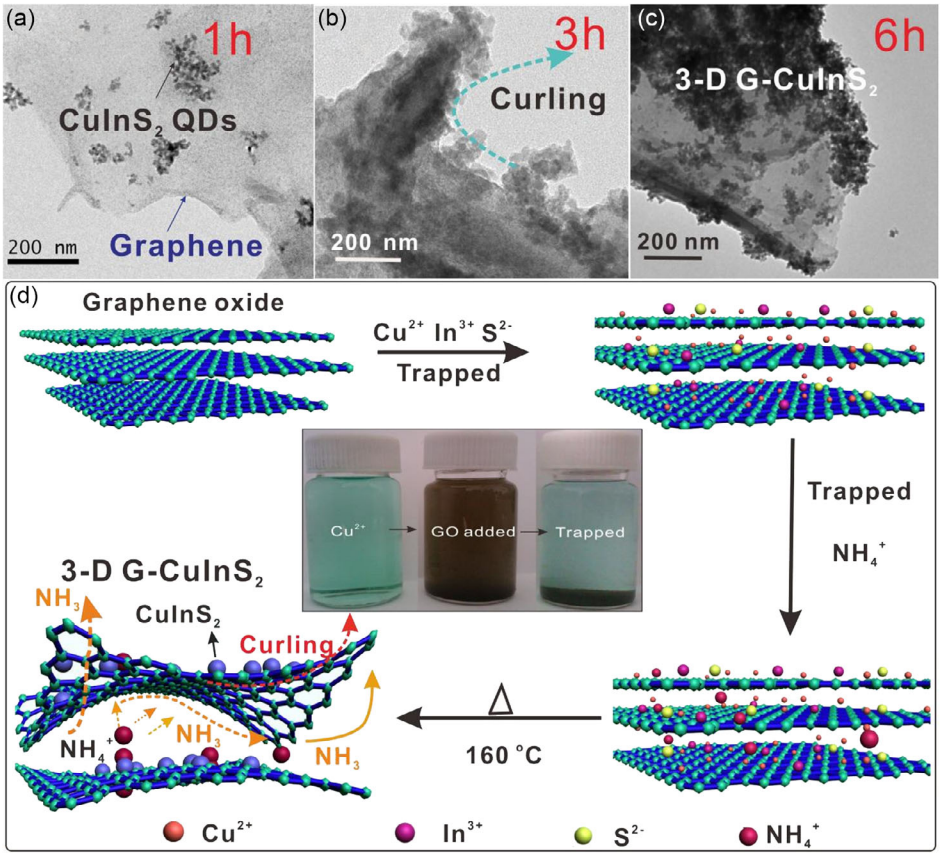

Figure 2. Morphology studies for the formation of 3D G–$CuInS_2$ composites at different reaction times of a) 1 h, b) 3 h, and c) 6 h. d) The schematic diagram of trapping of Cu^{2+}, In^{3+}, S^{2-}, and NH_4^+, respectively, and follow-on hydrothermal process for the formation of 3D G–$CuInS_2$ composites. The inset of (d) shows the picture illustrating ion-trapping phenomenon.

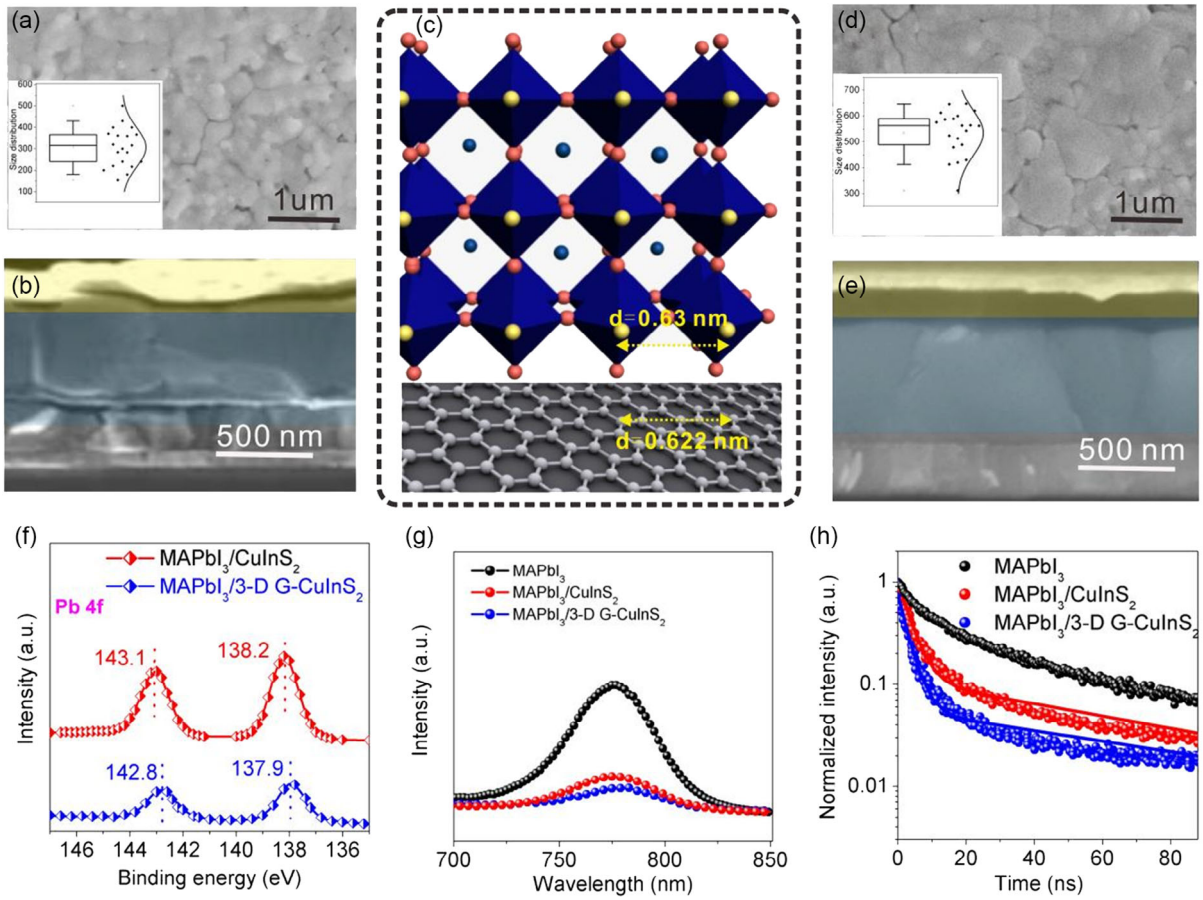

Figure 3. Characterization of $MAPbI_3$ thin films. a) Top view and b) cross section of SEM images of the $MAPbI_3$ crystals on pristine $CuInS_2$. c) Schematic structure of graphene bridging $MAPbI_3$ crystals. d) Top view and e) cross section of SEM images of $MAPbI_3$ crystals on 3D G–$CuInS_2$. f) The XPS spectra of the samples. g) PL spectra of the thin films (ex = 475 nm) and h) TRPL (λex = 560 nm, monitored at 775 nm). The inset in (a,b): the $MAPbI_3$ size distribution patterns.

200–400 nm from their images (Figure 3a and S4a, Supporting Information), while $MAPbI_3$ on 3D G–$CuInS_2$ substrate presents grain boundary of 400–700 nm, which is about two times of the $CuInS_2$ substrate-based crystal size (Figure 3d and S4b,c, Supporting Information). Besides, the cross-section image of the $MAPbI_3$ thin film on 3D G–$CuInS_2$ substrate (Figure 3b) is more compact than that on the counterpart substrate of pristine $CuInS_2$ (Figure 3e). The lattice spacing (0.63 nm) of $MAPbI_3$ crystal (100) is almost two times of that of graphene (0.31 nm) (Figure 3c).[24] The lattice matching of graphene and $MAPbI_3$ can suppress stress concentration during crystal growth and result in high-quality $MAPbI_3$ films with lower defect density.[25] In addition, the oxy- group (–O–) on the surface of graphene passivates the excess Pb in $MAPbI_3$, reducing the carrier recombination at the interface between $CuInS_2$ and $MAPbI_3$.

To verify the passivation of Pb, XPS results were recorded to identify the outermost orbital electron energy of Pb element in $MAPbI_3$. Through valence bond theory and molecular orbital theory, we know that the increase of external electron cloud density will lower binding energy of the element that can be reflected in shifted XPS peaks.[26] For $MAPbI_3$ crystals on pristine $CuInS_2$, the electrons on 4f orbit of Pb show two XPS peaks locating at 143.1 and 138.2 eV, respectively. However, the peak positions shift to 142.8 and 137.9 eV for $MAPbI_3$ on 3D G–$CuInS_2$, suggesting a strong interaction between graphene surface groups and Pb for passivation effects. The absorption spectra of the $MAPbI_3$ thin film on both substrates of native $CuInS_2$ and 3D G$CuInS_2$ are acquired (Figure S5, Supporting Information). Compared with that on pristine $CuInS_2$, the $MAPbI_3$ growth on 3D G–$CuInS_2$ shows a higher absorption intensity. Besides, their crystal structures were studied by means of XRD (Figure S6, Supporting Information), and stronger diffraction peaks of the $MAPbI_3$ crystals on 3D G–$CuInS_2$ are found, which imply better crystallinity in comparison with those of $MAPbI_3$ crystals on the pristine $CuInS_2$ QDs.

The photoluminescence (PL) study on $MAPbI_3$ film was performed to confirm the charge transfer process (Figure 3g). $MAPbI_3$ shows a broad band with peak emission at 775 nm, which is significantly quenched when in contact with $CuInS_2$ QDs, indicating an effective charge transfer process occurring between the $MAPbI_3$ layer and $CuInS_2$ QDs.[27] The PL quenching of $MAPbI_3$ is furthermore increased after contacting with 3D G–$CuInS_2$ film, implying a more facilitated charge transfer behavior at the interface between $MAPbI_3$ and 3D G–$CuInS_2$

film. To confirm that, TRPL of the thin films is measured (Figure 3h). As expected, the PL lifetime of $MAPbI_3$ is significantly reduced as a faster decay when in contact with 3D G–$CuInS_2$ thin film (Table S1, Supporting Information), indicating the facilitated electron injection efficiency at the interface between $MAPbI_3$ crystal and 3D G–$CuInS_2$ thin film.

The energy bands of $CuInS_2$ and 3D G–$CuInS_2$ are measured by the direct-bandgap method and ultraviolet photoelectron spectroscopy (UPS) (Figure S7, Supporting Information). The energy bandgaps (E_g) of 1.75 and 1.79 eV are found for pristine $CuInS_2$ QDs and 3D G–$CuInS_2$, respectively. The onset of the UPS spectra is applied to determine the distance between Fermi level (E_f) and the valence band (E_{VB}), where ($E_f - E_{VB}$) is estimated to be 2.32 eV for pristine $CuInS_2$ QDs.[28] The Fermi level can be determined by the D-value between cutoff edge of the UPS spectrum as 21.22 eV, leading to calculated E_f of −3.45 eV for pristine $CuInS_2$ QDs. Thus, the conductive band levels (E_{CB}) and E_{VB} of $CuInS_2$ QDs are calculated to be −4.07 and −5.77 eV, respectively. For comparison, the E_{CB} and E_{VB} of the 3D G–$CuInS_2$ are measured to be -3.98 and -5.77 eV. This result shows the law that the smaller the QD particle, the wider the E_g. The details of energy band parameters of $CuInS_2$ and 3D G–$CuInS_2$ are listed in Table S2, Supporting Information.

Based on the UPS results, the energy-level diagram is given in **Figure 4**a. The E_{CB} value of 3.98 eV for 3D G–$CuInS_2$ provides favorable energy level for electron transport, where the electrons generated by $MAPbI_3$ crystal can be injected into the 3D G–$CuInS_2$ efficiently. The transmittance spectra of 3D G–$CuInS_2$ and G–$CuInS_2$ thin films are measured (Figure S8, Supporting Information). The comparable transmission of 88.2% and 89.5% between 3D G–$CuInS_2$ is G–$CuInS_2$ which clearly demonstrates that graphene does not affect the optical transparency of the thin films. The contact angle of $MAPbI_3$ solution on 3D G–$CuInS_2$ thin film is smaller than that of the solution on the pristine one ($CuInS_2$) (Figure S9, Supporting Information). Thus, perovskite solution on the 3D G–$CuInS_2$ substrate is more prone to nucleation, leading to a denser and highly crystalline crystal.[29]

Solar cells based on 3D G–$CuInS_2$ and $CuInS_2$ QDs were fabricated with their schematic device diagram, as displayed in Figure S10, Supporting Information. As shown in Figure 4b, the champion device based on $CuInS_2$ QDs shows an open-circuit voltage (V_{oc}) of 1.09 V, a short-circuit current density (J_{sc}) of 22.5 mA cm^{-2}, and a fill factor (FF) of 0.79, leading to its PCE of 19.5%. Nevertheless, the champion device based on 3D G–$CuInS_2$ achieves improved photovoltaic performance with a V_{oc} of 1.12 V, a J_{sc} of 24.3 mA cm^{-2}, FF of 0.82, and a consequent PCE of 22.4%. All the device parameters for the 3D G–$CuInS_2$-based solar cells exhibit noticeable increases, especially the PCE increases by 14.8% in comparison with the pristine $CuInS_2$ counterpart-based ones. Simultaneously, the 3D G–$CuInS_2$-based solar cells almost have a negligible hysteresis with its remarkably lower hysteresis factor of 0.035 than that of $CuInS_2$-based ones (0.062) (Table S3, Supporting Information). Besides, we record their PV performance from 20 devices based on $CuInS_2$ and 3D G–$CuInS_2$, respectively, with their standard deviations reported (Figure S11, Table S4 and S5, Supporting Information), proving excellent reproducibility of the devices based on 3D G–$CuInS_2$.

The EQE spectra and the integrated J_{sc} of 3D G–$CuInS_2$ and $CuInS_2$ QDs-based solar cells are recorded (Figure 4c) to present their current intensities. Compared with $CuInS_2$ QD-based

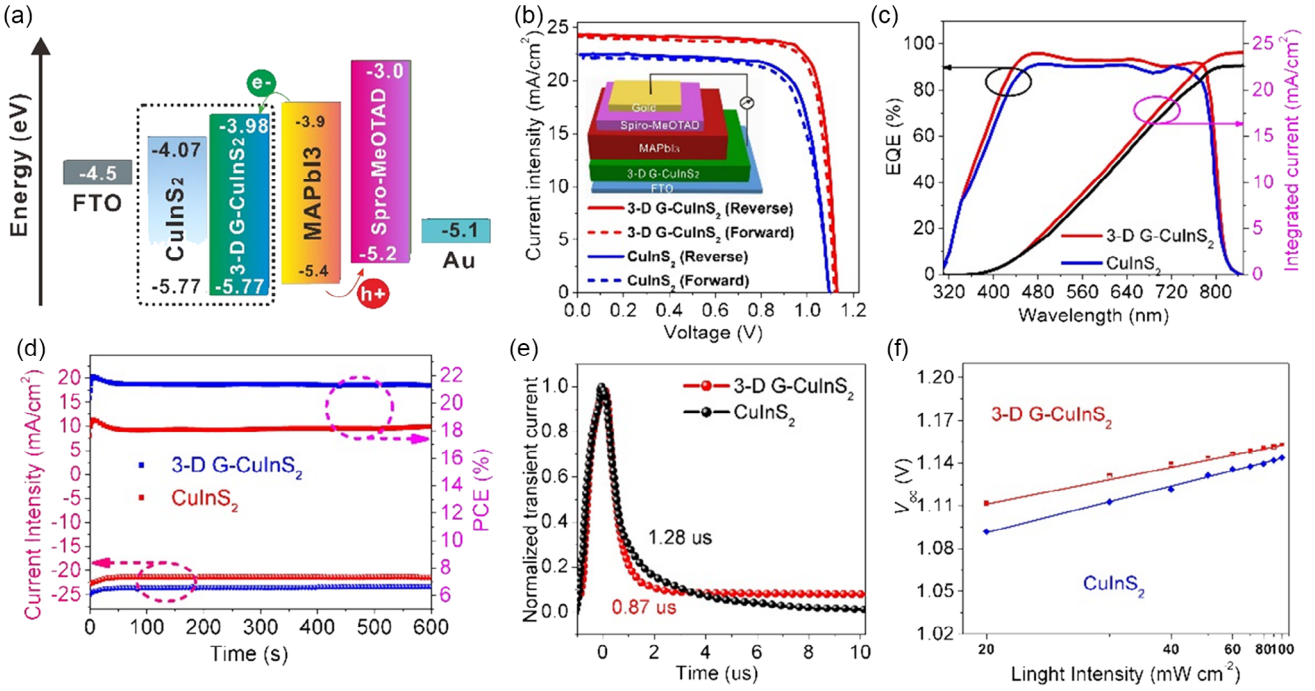

Figure 4. a) The energy-level diagram of the solar cells based on $CuInS_2$ and 3D G–$CuInS_2$. b) *J–V* curves of the solar cells. c) The EQE– and integrated current–curves of the solar cells. d) The steady-state current density and PCE versus time for the best-performing devices that are $CuInS_2$- and 3D G–$CuInS_2$-based, respectively. e) Transient photocurrent decay curves. f) Light intensity-dependent V_{oc} of the $CuInS_2$ and 3D G–$CuInS_2$-based devices.

device, the EQE value of 3D G–$CuInS_2$-based one increases in the whole region. The highest EQE of 93.7% and integrated J_{sc} of 24.1 mA cm^{-2} for 3D G–$CuInS_2$-based solar cell are clearly presented, respectively, which are reasonably higher than those of $CuInS_2$ QDs-based ones (90.7% and 22.6 mA cm^{-2}), proving very effectively promoted generation of photocurrent for the former system.

The steady-state PCE and photocurrent output at the maximum power point are recorded to confirm the efficiency champion devices (Figure 4d). Compared with $CuInS_2$ QD-based device, the 3D G–$CuInS_2$-based one shows an improved PCE and photocurrent output. These results are very close to the measured values from the *J–V* curves. In order to consider the carrier extraction capability of the device in the working state, the photocurrent and photovoltage decay curves are measured. In Figure 4e, the photocurrent decay time for 3D G–$CuInS_2$-based solar cell under short-circuit conditions is reduced to 0.87 µs, compared with 1.28 µs for pristine $CuInS_2$-based one. The excellent carrier extraction capability of 3D G–$CuInS_2$ reduced carrier extraction time by 1.47 times, which benefits the efficient carrier separation and extraction. In addition, the 3D G–$CuInS_2$ solar cell exhibited a longer electron lifetime of 4.5 µs (Figure S12, Supporting Information) in comparison to pristine $CuInS_2$ (2.6 µs), indicating a suppressed interfacial nonradiative recombination in 3D G–$CuInS_2$-based solar cells. Generally speaking, a suppressed charge recombination loss would result in an increased V_{oc}.[30,31] The light intensity-dependent V_{oc} measurement is applied to test nonradiative recombination (Figure 4f). The diode ideal factor (n) is calculated by Equation (1).[32]

$$V_{oc} = \frac{nKT\ln(I)}{q} + C \tag{1}$$

where T, K, q, and I represent the temperature, Boltzmann constant, elementary charge, and light intensity, respectively. The value of linear slope reflects the nonradiative recombination mechanism in an inverse manner.[12,33] The linear slope in 3D G–$CuInS_2$-based device is lower than that in the pristine $CuInS_2$

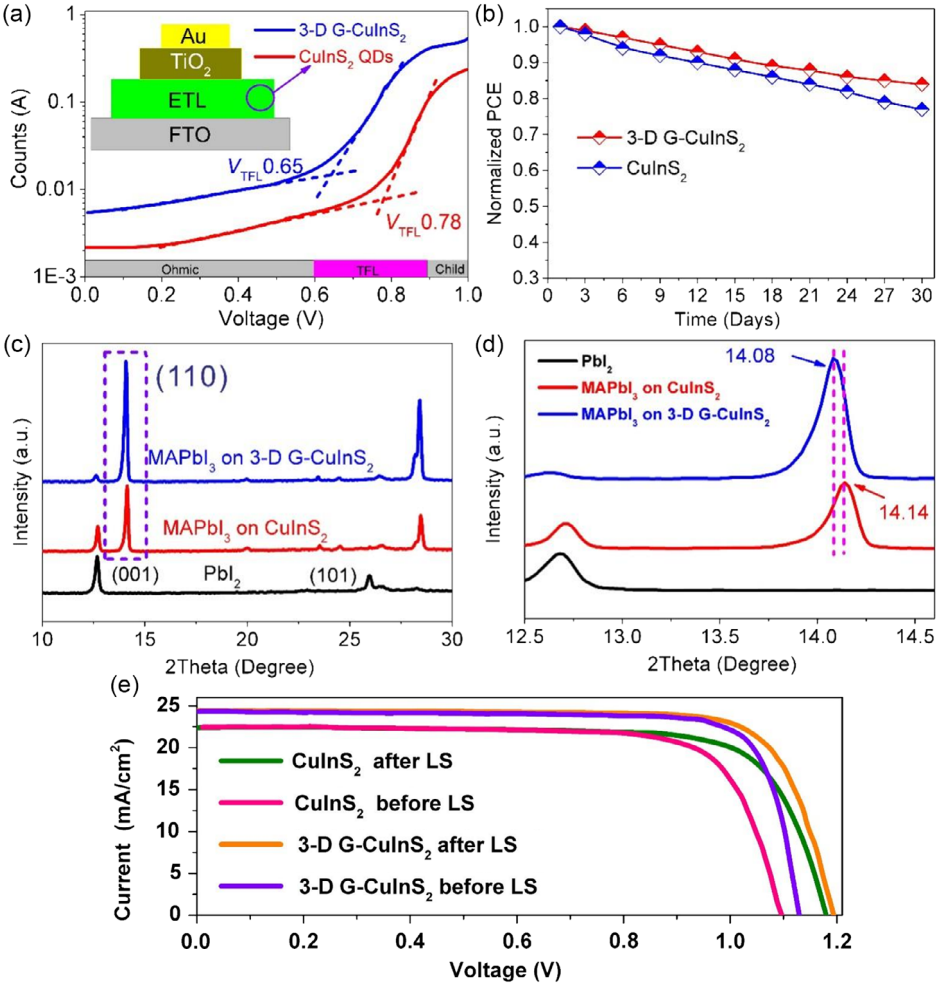

Figure 5. a) Dark J–V curves of electron-only devices based on $CuInS_2$ and 3-D G-$CuInS_2$. b) Long-term stability of the pristine $CuInS_2$ and 3D G–$CuInS_2$-based solar cells in air (relative humidity of 25%) at room temperature without encapsulation. c) XRD patterns of the $MAPbI_3$ crystal from the pristine $CuInS_2$ and 3D G–$CuInS_2$ solar cells in air for 30 days. d) The amplification of (110) peak of $MAPbI_3$ crystal in (c). The inset in (a) shows the schematic device diagram of the electron-only devices based on $CuInS_2$ and 3D G–$CuInS_2$. e) The *J–V* characteristics of devices based on $CuInS_2$ and 3D G–$CuInS_2$ before and after LS under AM 1.5 G solar illumination.

counterpart, suggesting the suppressed trap-assisted nonradiative recombination in 3D G–$CuInS_2$-based solar cells.

The space–charge-limited current (SCLC) method was adopted to study the trap density of thin films. When the applied voltage exceeds the trap-filled limit voltage (V_{TFL}), the current is significantly enhanced. The trap density (n_{trap}) can be calculated by Equation (2).[34]

$$n_{trap} = \frac{2\varepsilon\varepsilon_0 V_{TFL}}{eL^2} \quad (2)$$

where L is the thickness of the $MAPbI_3$ crystal layer, ε_0 denotes the vacuum dielectric constant, and ε represents the relative dielectric constant. The electron-only devices were fabricated (**Figure 5**a). The J–V curves were measured in the dark with the bias voltage at region from 0 to 3 V. The V_{TFL} for the pristine $CuInS_2$ and 3D G–$CuInS_2$-based devices were 0.78 and 0.65 V, respectively. The V_{TFL} is proportional to n_{trap}, as other factors remained unchanged. Thus, the n_{trap} in 3D G–$CuInS_2$ based device is lower than that in its counterpart.

The air stability of pristine $CuInS_2$ and 3D G–$CuInS_2$-based solar cells was evaluated, respectively (Figure 5b). The device based on 3D G–$CuInS_2$ shows better stability than the pristine $CuInS_2$ counterpart, maintaining over 85% of the initial efficiency after 30 days. However, the pristine $CuInS_2$-based counterpart suffers noticeably faster degradation which maintains only 76% of its original efficiency. The results demonstrates that 3D G–$CuInS_2$-based solar cell possesses excellent long-term stability. The XRD patterns are recorded to further investigate the crystal decomposition for the pristine $CuInS_2$ and 3D G–$CuInS_2$-based solar cells in air for 30 days (Figure 5c). Obviously, the $MAPbI_3$ thin film on 3D G–$CuInS_2$ shows lower intensity of PbI_2 peak compared to that on the counterpart, indicating better crystal stability for $MAPbI_3$ crystal growth on 3D G–$CuInS_2$ than that on pristine $CuInS_2$. Generally speaking, the lattice matching of crystal and 2D materials can reduce the stress concentration during the preparation process.[35] As shown in Figure 5d, the 2θ location of (110) peak of $MAPbI_3$ crystal on 3D G–$CuInS_2$ is shifted from 14.14° (that of $MAPbI_3$ crystal on pristine $CuInS_2$) to 14.08°, suggesting that the strong interactions between $MAPbI_3$ crystal and 3D G–$CuInS_2$ at their interfaces eliminate the stress during the growth of the $MAPbI_3$ crystal. Finally, the light soaking (LS) effect on device performance was investigated. As shown in Figure 5e, after about 30 min LS, the PCE for both of the 3D G–$CuInS_2$ and $CuInS_2$-based solar cells is improved, indicating their excellent LS stability.

3. Conclusion

We presented an effective strategy to improve PSCs by means of applying a novel passivate ETL layer from newly designed 3D G–$CuInS_2$ composites. The introduction of graphene reduces the influence of aggregation of $CuInS_2$ QDs on the $MAPbI_3$ film formation and passivates the interface between them. The lattice matching of graphene and $MAPbI_3$ inhibits the concentrated stress generated during the growth of perovskite resulting crystal films with large grain boundaries. Besides, the surface electron defect density in 3D G–$CuInS_2$ composite is much lower than that in pristine $CuInS_2$ QDs, and the 3D structure enhances the electron transport from perovskite film to $CuInS_2$ QDs, which greatly promotes the electron transmission and reduces the recombination loss. The PL and TRPL study demonstrate a facilitated electron injection efficiency at the interface between $MAPbI_3$ crystal and 3D G–$CuInS_2$ thin film in comparison to the pristine $CuInS_2$ QDs. In addition, 3D G–$CuInS_2$ shows excellent carrier extraction capability of reducing carrier extraction time by 1.47 times than the counterpart. Correspondingly, a high device J_{sc} of 24.3 mA cm^{-2} based on 3D G–$CuInS_2$ is achieved and a consequent PCE of 22.4% is obtained. Compared with the pristine $CuInS_2$-based solar cell, the 3D G–$CuInS_2$-based one increases its PCE by 15%, which also shows a higher long-term stability, maintaining 85% of its original efficiency in the air atmosphere for 30 days without encapsulation. This work provides a new reference for the preparation of highly efficient PSCs by passivating the bottom of crystal films and promotes the application and research of graphene-based new materials in PSCs

Supporting Information

Supporting Information is available from the Wiley Online Library or from the author.

Acknowledgements

This work was supported by the Innovation Platform Fund of Hunan Education Department (grant no.: 20K115) and Natural Science Foundation of Hunan Province (grant no.: 2019JJ50558). J.C. acknowledges financial support from Scientific Research Fund of Hunan Provincial Education Department (21B0447). D.Y. thanks financial support from Sino-Danish Centre for Education and Research (SDC).

Conflict of Interest

The authors declare no conflict of interest.

Data Availability Statement

The data that support the findings of this study are available in the supplementary material of this article.

Keywords

electron transport layers, interfacial engineering, passivation, perovskite solar cells

Received: March 3, 2023
Revised: April 4, 2023
Published online: May 10, 2023

[1] J. Jeong, M. Kim, J. Seo, H. Lu, P. Ahlawat, A. Mishra, Y. Yang, M. A. Hope, F. T. Eickemeyer, M. Kim, Y. J. Yoon, I. W. Choi, B. P. Darwich, S. J. Choi, Y. Jo, J. H. Lee, B. Walker, S. M. Zakeeruddin, L. Emsley, U. Rothlisberger, A. Hagfeldt, D. S. Kim, M. Grätzel, J. Y. Kim, *Nature* **2021**, *592*, 381.
[2] M. Kim, J. Jeong, H. Lu, T. K. Lee, F. T. Eickemeyer, Y. Liu, I. W. Choi, S. J. Choi, Y. Jo, H.-B. Kim, S.-I. Mo, Y.-K. Kim, H. Lee, N. G. An,

S. Cho, W. R. Tress, S. M. Zakeeruddin, A. Hagfeldt, J. Y. Kim, M. Grätzel, D. S. Kim, *Science* **2022**, *375*, 302.
[3] K. Sveinbjörnsson, B. Li, S. Mariotti, E. Jarzembowski, L. Kegelmann, A. Wirtz, F. Frühauf, A. Weihrauch, R. Niemann, L. Korte, F. Fertig, J. W. Müller, S. Albrecht, *ACS Energy Lett.* **2022**, *7*, 2654.
[4] Q. Jiang, J. Tong, Y. Xian, R. A. Kerner, S. P. Dunfield, C. Xiao, R. A. Scheidt, D. Kuciauskas, X. Wang, M. P. Hautzinger, R. Tirawat, M. C. Beard, D. P. Fenning, J. J. Berry, B. W. Larson, Y. Yan, K. Zhu, *Nature* **2022**, *611*, 278.
[5] J. Yang, S. C. Cho, S. Lee, J. W. Yoon, W. H. Jeong, H. Song, J. T. Oh, S. G. Lim, S. Y. Bae, B. R. Lee, M. Ahmadi, E. H. Sargent, W. Yi, S. U. Lee, H. Choi, *ACS Nano* **2022**, *16*, 1649.
[6] Q. Jiang, Y. Zhao, X. Zhang, X. Yang, Y. Chen, Z. Chu, Q. Ye, X. Li, Z. Yin, J. You, *Nat. Photon.* **2019**, *13*, 460.
[7] P. Zhang, J. Wu, T. Zhang, Y. Wang, D. Liu, H. Chen, L. Ji, C. Liu, W. Ahmad, Z. D. Chen, S. Li, *Adv. Mater.* **2018**, *30*, 1703737.
[8] C. H. Lin, L. Hu, X. Guan, J. Kim, C. Y. Huang, J. K. Huang, S. Singh, T. Wu, *Adv. Mater.* **2022**, *34*, 2108616.
[9] F. Gao, K. Liu, R. Cheng, Y. Zhang, *Appl. Surf. Sci.* **2020**, *528*, 146560.
[10] Y. Ding, B. Ding, H. , O. J. Usiobo, T. Gallet, Z. Yang, Y. Liu, H. Huang, J. Sheng, C. Liu, Y. Yang, V. I. E. Queloz, X. Zhang, J. N. Audinot, A. Redinger, W. Dang, E. Mosconic, W. Luo, F. De Angelis, M. Wang, P. Dorflinger, M. Armer, V. Schmid, R. Wang, K. G. Brooks, J. Wu, V. Dyakonov, G. Yang, S. Dai, P. J. Dyson, et al., *Nat. Nanotechnol.* **2022**, *17*, 598.
[11] F. Gao, H. Dai, H. Pan, Y. Chen, J. Wang, Z. Chen, *J. Colloid Interface Sci.* **2018**, *513*, 693.
[12] W. Hong, F. Gao, C. Zhang, X. Zhou, X. Deng, S. Jiang, S. Yin, *Colloid Surface A* **2022**, *646*, 128958.
[13] F. Gao, W. Hong, Z. Zhao, C. Zhang, X. Deng, Y. Zhang, *Nanoscale* **2023**, *15*, 490.
[14] Q. Dong, M. Wang, Q. Zhang, F. Chen, S. Zhang, J. Bian, T. Ma, L. Wang, Y. Shi, *Nano Energy* **2017**, *38*, 358.
[15] L. Xiong, Y. Guo, J. Wen, H. Liu, G. Yang, P. Qin, G. Fang, *Adv. Funct. Mater.* **2018**, *28*, 1802757.
[16] Q. Jiang, X. Zhang, J. You, *Small* **2018**, *14*, 1801154.
[17] Y.-Q. Zhou, B.-S. Wu, G.-H. Lin, Z. Xing, S.-H. Li, L.-L. Deng, D.-C. Chen, D.-Q. Yun, S.-Y. Xie, *Adv. Energy Mater.* **2018**, *8*, 1800399.
[18] F. Gao, Q. Zheng, Y. Zhang, *ACS Omega* **2019**, *4*, 3432.
[19] X. H. Xu, F. Wang, J. J. Liu, K. C. Park, M. Fujishige, *Sol. Energy Mater. Sol. Cells* **2011**, *95*, 791.
[20] G. Yang, C. Chen, F. Yao, Z. Chen, Q. Zhang, X. Zheng, J. Ma, H. Lei, P. Qin, L. Xiong, W. Ke, G. Li, Y. Yan, G. Fang, *Adv. Mater.* **2018**, *30*, 1706023.
[21] L. M. Malard, M. A. Pimenta, G. Dresselhaus, M. S. Dresselhaus, *Phys. Rep.* **2009**, *473*, 51.
[22] C. Wu, W. Fang, Q. Cheng, J. Wan, R. Wen, Y. Wang, Y. Song, M. Li, *Angew. Chem. Int. Ed. Engl.* **2022**, *61*, e202210970.
[23] H. Wang, J. T. Robinson, G. Diankov, H. Dai, *J. Am. Chem. Soc.* **2010**, *132*, 3270.
[24] Q. Cao, J. Yang, T. Wang, Y. Li, X. Pu, J. Zhao, Y. Zhang, H. Zhou, X. Li, X. Li, *Energy Environ. Sci.* **2021**, *14*, 5406.
[25] A. Yang, Y. Li, C. Yang, Y. Fu, N. Wang, L. Li, F. Yan, *Adv. Mater.* **2018**, *30*, 1800051.
[26] J. Li, T. Jiu, S. Chen, L. Liu, Q. Yao, F. Bi, C. Zhao, Z. Wang, M. Zhao, G. Zhang, Y. Xue, F. Lu, Y. Li, *Nano Lett.* **2018**, *18*, 6941.
[27] P. Zeng, X. Ren, L. Wei, H. Zhao, X. Liu, X. Zhang, Y. Xu, L. Yan, K. Boldt, T. A. Smith, M. Liu, *Angew. Chem. Int. Ed. Engl.* **2022**, *61*, 202111443.
[28] F. Wang, M. Yang, Y. Zhang, J. Du, D. Han, L. Yang, L. Fan, Y. Sui, Y. Sun, X. Meng, J. Yang, *Chem. Eng. J.* **2020**, *402*, 126303.
[29] W. Hui, Y. Yang, Q. Xu, H. Gu, S. Feng, Z. Su, M. Zhang, J. Wang, X. Li, J. Fang, F. Xia, Y. Xia, Y. Chen, X. Gao, W. Huang, *Adv. Mater.* **2020**, *32*, 1906374.
[30] I. M. Hermes, Y. Hou, V. W. Bergmann, C. J. Brabec, S. A. L. Weber, *J. Phys. Chem. Lett.* **2018**, *9*, 6249.
[31] Y. Hu, E. M. Hutter, P. Rieder, I. Grill, J. Hanisch, M. F. Aygüler, A. G. Hufnagel, M. Handloser, T. Bein, A. Hartschuh, K. Tvingstedt, V. Dyakonov, A. Baumann, T. J. Savenije, M. L. Petrus, P. Docampo, *Adv. Energy Mater.* **2018**, *8*, 1703057.
[32] N. Li, A. Feng, X. Guo, J. Wu, S. Xie, Q. Lin, X. Jiang, Y. Liu, Z. Chen, X. Tao, *Adv. Energy Mater.* **2021**, 2103241.
[33] M. Li, F. Igbari, Z.-K. Wang, L.-S. Liao, *Adv. Energy Mater.* **2020**, *10*, 2000641.
[34] F. Hou, Y. Li, L. Yan, B. Shi, N. Ren, P. Wang, D. Zhang, H. Ren, Y. Ding, Q. Huang, T. Li, Y. Li, Y. Zhao, X. Zhang, *Sol. RRL* **2021**, *5*, 2100357.
[35] K. S. Novoselov, A. Mishchenko, A. Carvalho, A. H. Castro Neto, *Science* **2016**, *353*, aac9439.